INTERNATIONAL JOURNAL FOR NUMERICAL METHODS IN FLUIDS
*Int. J. Numer. Meth. Fluids* 2008; **57**:519–529
Published online 1 May 2007 in Wiley InterScience (www.interscience.wiley.com). DOI: 10.1002/fld.1500

# The spectral/*hp* element modelling of steady flow in non-planar double bends

K. E. Lee[1,2], K. H. Parker[1], C. G. Caro[1] and S. J. Sherwin[2,*,†]

[1]*Bioengineering, Imperial College London, London, U.K.*
[2]*Department of Aeronautics, Imperial College London, London, U.K.*

SUMMARY

The purpose of this study is to better understand steady flow in three-dimensional non-planar double bend geometries which are chosen to loosely model a right coronary or femoral artery, neglecting branches. The knowledge gained from idealized geometries can subsequently be applied to anatomically correct geometries. The three-dimensional computations of steady flows in planar and non-planar double bends at Reynolds numbers of 125 and 500 were performed using a high accuracy, spectral/*hp* element Navier–Stokes solver. In this study, we analyse the haemodynamics in terms of various mechanical factors (i.e. axial velocity, secondary flows, vorticity and coherent vortical structures). Although the effects of curvature and non-planarity on the flows are complex and often non-intuitive, from the numerical results, we can simplify and anticipate the secondary flow patterns, and by associations the wall shear stress distribution, in various double bend geometries with different non-planarities at physiological Reynolds number ($100 \leqslant Re \leqslant 500$). Non-planarity has the biggest effects on mixing and swirling of flow as observed through the coherent vortical structures and asymmetric secondary flow streamlines. Copyright © 2007 John Wiley & Sons, Ltd.

Received 14 December 2006; Revised 6 March 2007; Accepted 8 March 2007

KEY WORDS: spectral/*hp* element method; haemodynamics; non-planarity; curvature; double bend

## 1. INTRODUCTION

It is broadly accepted that local haemodynamic factors play a critical role in the genesis, development and distribution of atherosclerosis and cardiovascular disease. Atherosclerosis can occur anywhere in arteries but is particularly prevalent on the inner wall of curved arteries and the outer wall of bifurcations. Cholesterol level [1–5], obesity, diet, smoking [6], drinking, diabetes [7] and

*Correspondence to: S. J. Sherwin, Department of Aeronautics, Imperial College London, London SW7 2AZ, U.K.
†E-mail: s.sherwin@imperial.ac.uk

Contract/grant sponsor: Henry Smith's Kensington Estate Charity
Contract/grant sponsor: EPSRC Turbulence Consortium
Contract/grant sponsor: EPSRC Advanced Research Fellowship

renal failure [8] are examples of systemic risk factors implicated in atherogenesis, re-stenoses of bypass graft. Among various risk factors, the concentration of cholesterol in blood has been considered the most important factor since the plaques are rich in lipid [1–3], and this has been studied experimentally in various animals by feeding them with a diet containing cholesterol [4, 5].

None of these risk factors, however, can explain the focal nature of atherosclerotic lesions. Haemodynamic factors can explain the distribution of atherosclerotic lesions within the arteries and, for this reason, it is broadly accepted that local haemodynamic factors play a critical role in conjunction with systemic risk factors to produce localized disease, genesis, development and distribution of arterial disease. It is therefore important to understand fluid dynamic factors such as flow behaviour, velocity patterns and wall shear distribution.

Many researchers have investigated pressure, velocity distributions, velocity gradient and the influence of steady and unsteady shear stresses and the gradient of wall shear stress in steady or unsteady flows on the wall or on the blood cell in vascular configurations [9–11]. These mechanical factors are involved in the accumulation of lipids, a cause of atherosclerosis. The effect of curvature was investigated for steady and laminar flow through a planar curved pipe analytically by Dean [12–14] and experimentally by John [15, 16]. Other analyses have been carried out for three-dimensional laminar flow through planar circular pipes with particular variations of curvature. Some authors have reported various numerical and experimental studies for a planar double reverse curved arterial geometry to suggest that lesion location at the inner curvature may be associated with secondary flows near the inner curvature [17–20].

Most previous works, however, assume the flows to be planar and/or two dimensional, whereas flows in vessels are commonly non-planar and three dimensional. There is a growing belief that the non-planarity of blood vessels can have a major influence on local haemodynamics in circulatory flows. As has been described in the review by Caro *et al.* [21], many investigators have focused on the non-planarity influence on flows in specific arterial locations: aortic arch [22–28], branching of superficial coronary arteries [29–31], bifurcation of aorta [32], branching of femoral artery [33], distal femoral artery [34, 35], idealized non-planar bifurcations [36, 37] and carotid siphon [38]. However, few studies have reported on the effect of non-planarity in non-branching vessels [20].

The purpose of this study of steady flow is to better understand the effects of geometrical configurations on the flow in double bend geometries which are chosen to loosely model a right coronary artery or a femoral artery, neglecting branches. The knowledge gained from idealized geometries can subsequently be applied to anatomically correct geometries such as a right coronary artery, femoral arteries or even double bend shaped bypass grafts caused by the occlusion of proximal host vessel. It may be also valuable in future investigations into the mechanisms of plaque vulnerability and the risk of atherosclerotic narrowing in non-branch vessels. Numerical models can be readily modified to study the effects of a given parameter such as the non-planar angles or artery diameter. Further, this simulation could greatly reduce the costs of predicting the relationship between blood flow and geometrical characteristics compared to experiments. In this study, we investigate the effect of non-planarity and curvature in non-planar, non-branched double-curved arterial geometries with an ‘s’ shape. In addition to axial velocity, we also present the secondary flow patterns and the coherent vortical structure as measured by the $\lambda_2$ flow isocontours [39].

## 2. NUMERICAL MODELS AND ASSUMPTIONS

Steady flow in double bends is studied in the series of idealistic geometries shown in Figure 1. The diameter ($D$) of the bend and the radius ($R$) of curvature of the bends ($R = 2D$) were chosen



DOI: 10.1002/fld

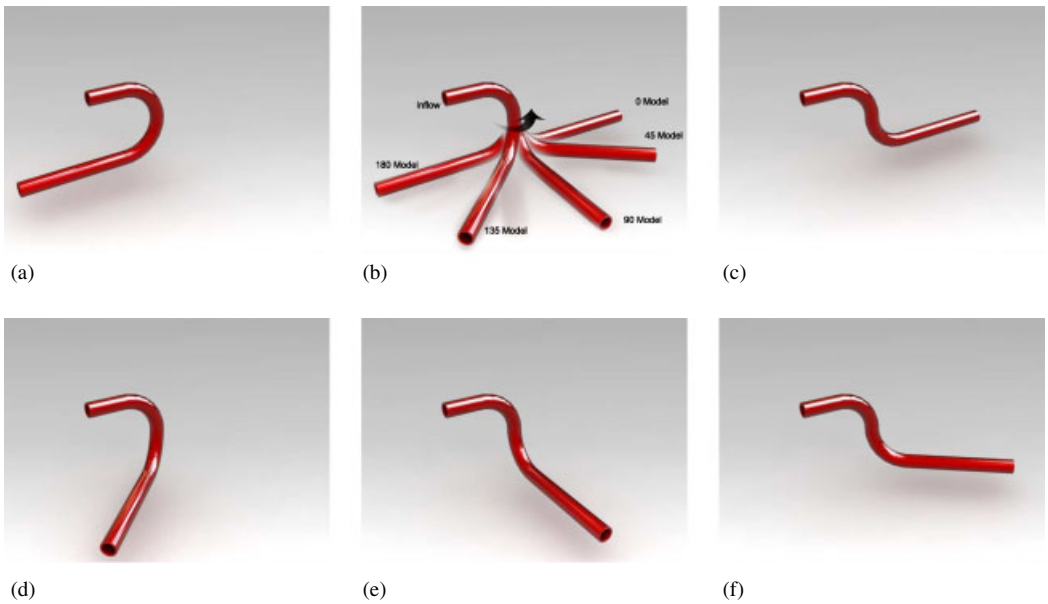


Figure 1. (a) 180° model; (b) all five models; (c) 0° model; (d) 135° model; (e) 90° model; and (f) 45° model.

to correspond to physiologically realistic vessels, particularly the right coronary artery. The CFD model consists of a straight inflow region, a double bend of two consecutive reverse quarters toroidal bends. In non-planar models, the second consecutive toroidal bend has the same radius of curvature but lies out of the plane of curvature of the original bend with azimuthal angles $\phi = 45°$, $\phi = 90°$ and $\phi = 135°$ as shown in Figures 1(f), (e) and (d) respectively. The straight outlet region is of length 8D. In addition, we consider two other models which lie in the same plane; the second bend of the 0° model, as shown in Figure 1(c), has opposite curvature to the original bend in a single plane and the other planar model is a single U-bend which we refer to as the 180° model, as shown in Figure 1(a). By comparing flows in the three non-planar models against flows in the standard planar double bends, we will identify the effect of non-planarity. Steady flow in a curved tube is characterized by both the Reynolds number and the Dean number ($4\sqrt{D/R}Re$). In these five models, steady flow was studied at Reynolds number 125 and 500 (Dean number $D = 354$ and 1414), which correspond to the Reynolds number in medium sized human arteries based on the mean and peak velocity numerical models [40]. We make the following assumptions: Newtonian blood flow and negligible effect of distensibility of the arterial walls. The boundary conditions are: no-slip on the pipe wall, zero velocity gradients and zero pressure at the outlet and Poiseuille velocity profile at the inflow.

## 3. NUMERICAL METHODOLOGY

The mesh generation was accomplished with an advancing front method [41]. A modified advancing layers method was employed near the pipe wall to generate a prismatic boundary layer mesh and



DOI: 10.1002/fld

then the advancing front method was applied to construct a mesh for the rest of the domain from the boundary layer towards its interior by a three-dimensional tetrahedral volume mesh [41]. The numerical simulations have been performed using an incompressible Navier–Stokes equation solver, which is based on spectral/*hp* element discretization in space [42]. This discretization uses hybrid-shaped spectral elements and a hierarchical expansion basis, which produces well-conditioned matrix systems for high-order polynomial expansions.

We take the governing incompressible Navier–Stokes equations,

$$f(\mathbf{u}) = -\frac{\partial \mathbf{u}}{\partial t} - \mathbf{u} \cdot \nabla \mathbf{u} - \nabla p + \nu \nabla^2 \mathbf{u} = 0$$

with the continuity requirement

$$\nabla \cdot \mathbf{u} = 0$$

where $\mathbf{u}$ is the three-dimensional velocity field, $p$ is the fluid kinematic pressure and $\nu$ is the kinematic viscosity. The starting point for the spectral/*hp* element method is the approximation of the differential equation which is formulated into an integral form with respect to the scheme expansion basis (i.e. a Galerkin projection), such that

$$\int_{\Omega} w(f(\mathbf{u}^{\delta}) - f(\mathbf{u}))\, \mathrm{d}\Omega = 0 \tag{1}$$

where $\Omega$, $w$, $\mathbf{u}^{\delta}$ and $\mathbf{u}$ denote the solution domain, weighted functions, approximated solutions and exact solutions, respectively. The resulting integro-differential equation is then approximated

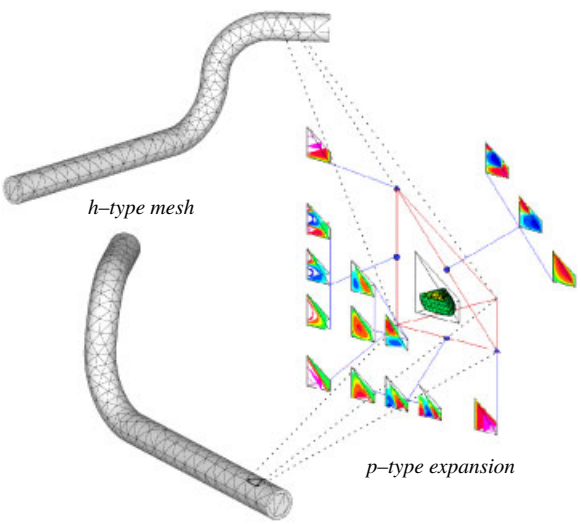


Figure 2. Spectral/*hp* element discretization using *h*-type macro-elements and *p*-type Jacobi-based polynomial expansions. The modes shown here are representative of a fourth-order expansion within each tetrahedral element.



DOI: 10.1002/fld

in space as

$$\mathbf{u}^{\delta} = \sum_{i=0}^{N_{dof}-1} \Phi_i \mathbf{u}_i = \sum_{e=0}^{N_{el}} \sum_{p=0}^{O(P^3)} \phi_p^e \mathbf{u}_p^e$$

where $\Phi_i$ and $\phi_i$ denotes the global mode and the local mode of basis functions or expansion functions. Substitution of this approximation into Equation (1) leads to a linear algebraic system which can be solved to obtain the coefficients $u_i$.

A spectral/$hp$ element discretization is a high-order discretization methods combining both $h$-type and $p$-type refinement methods where the number of sub-domains and polynomial order within the elements can be independently varied. In this study, a modal hybrid spectral/$hp$ element method was applied based upon Jacobi-family polynomial as shown in Figure 2. The solutions in the non-planar double bend geometries are computed on mesh with approximately 1500 spectral elements with $P = 5$th-, 8th- and 10th-order polynomial expansions, which corresponds to a maximum of 52 500, 180 000 and 330 000 local degrees of freedom per variable.

## 4. DATA ANALYSIS TECHNIQUE FOR VORTICAL STRUCTURES

Vortical motion in coherent structures helps us to understand separated flow phenomena like entrainment and mixing, heat and mass transfer [43]. Jeong and Hussain introduced a $\lambda_2$ definition of a vortex in an incompressible flow in terms of the eigenvalues of the symmetric tensor $S^2+\Omega^2$ to obtain a better indicator for the existence of a vortex [39]. Coherent vortical structure corresponds to the region of negative $\lambda_2$, where $\lambda_2$ is the second largest eigenvalue of $S^2 + \Omega^2$, where $S$ and $\Omega$ are the symmetric and anti-symmetric parts of the velocity gradient tensor $\nabla\mathbf{u}$, i.e.

$$S = \tfrac{1}{2}[\nabla\mathbf{u} + (\nabla\mathbf{u})^{\mathrm{T}}], \quad \Omega = \tfrac{1}{2}[\nabla\mathbf{u} - (\nabla\mathbf{u})^{\mathrm{T}}]$$

Physically, the individual tensor $S$ represents stretching whilst the tensor $\Omega$ represents rotation.

## 5. RESULTS AND DISCUSSIONS

We will now consider the steady flow at $Re = 125$ and 500 in the five idealized geometries using a combination of velocity and vorticity sectional profiles and the vortical structure technique outlined in Section 4. The sections of interest are highlighted in Figure 3. All of the slices for the contours of axial velocity, transverse flow and vorticity are oriented so that they appear to an observer on the start of the vessel looking downstream. In Figure 3(b), we also highlight the orientations of each cross-section for a non-planar model (in this case, the 90° model). In displaying the sectional data, we display point $A$ at the top of each cross-section. However as seen in Figure 3(b) when we traverse along the pipe, the location of point $A$ within each circular cross-section will rotate in proportion to the angle of the model. So in the 90° model, point $A$ along the outflow pipe is rotated by a quarter turn (i.e. 90°) with respect to the sectional data at the inflow. Similarly in the 180° model at the outflow, the sectional data should be physically interpreted as being rotated by half a turn (180°).

In Figure 4 we show the 0° model case. The isocontour on the right shows the $\lambda_2$ isocontour in this geometry at $Re = 125$. Also shown in this figure are a series of axial velocities



DOI: 10.1002/fld

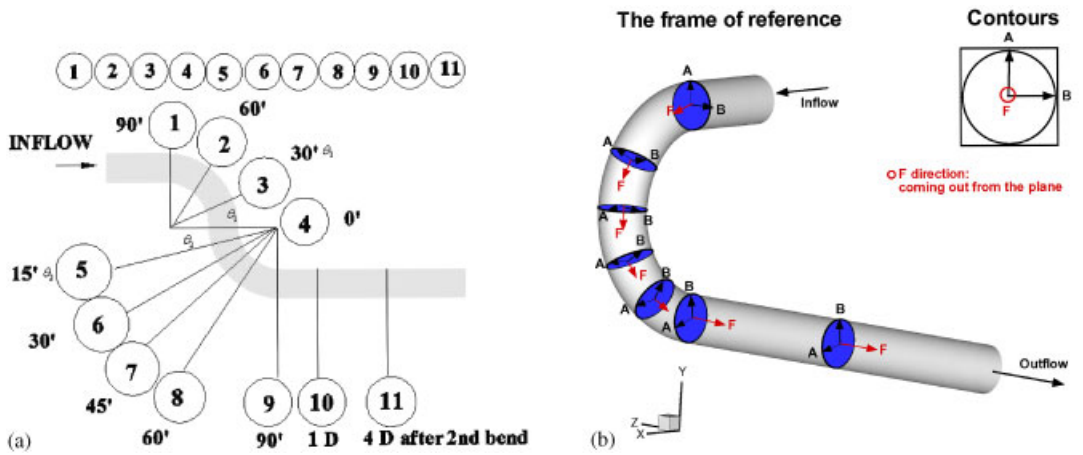


Figure 3. (a) Cross-sections evaluated in double bend geometries and (b) physical orientation of each section: points *A* and *B* follow a continuous line along the geometry, therefore these datum points will rotate within the section by the same amount as the angle associated with the model, in this case 90°.

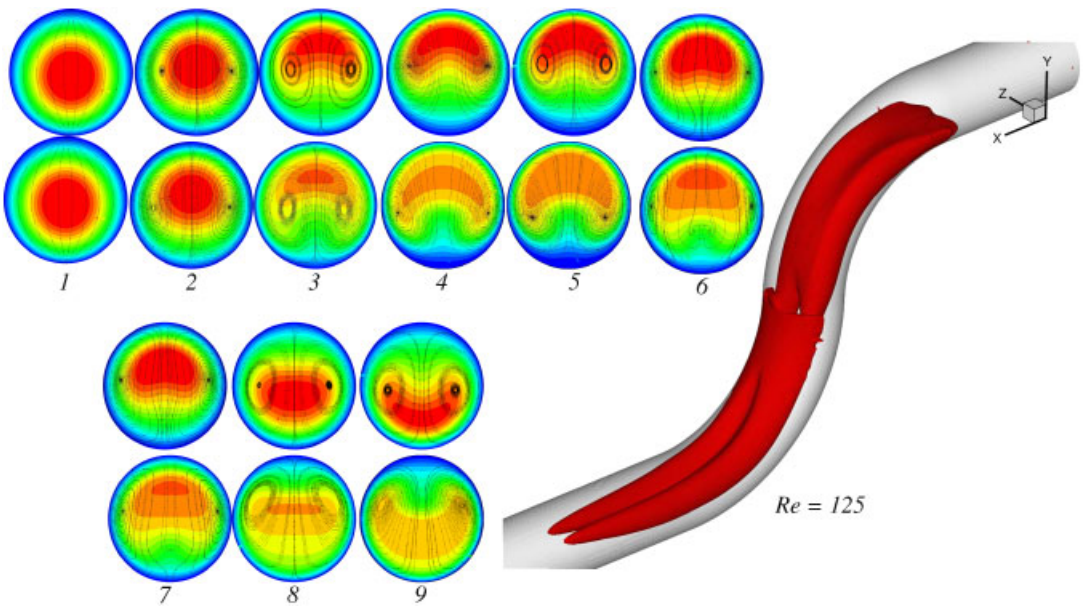


Figure 4. 0° model: the isocontour show the $\lambda_2$ coherent vortex structure at $Re = 125$, highlighting the two Dean vortex patterns set up in each quarter bend. The inset sections correspond to the numbering in Figure 3(a). The top and bottom series of slices show axial velocity at $Re = 125$ and 500, respectively.

with transverse streamlines indicated. The top series of slices is at $Re = 125$ and the bottom series of slices is at $Re = 500$. The location of each section (as numbered) is shown in Figure 3.



DOI: 10.1002/fld

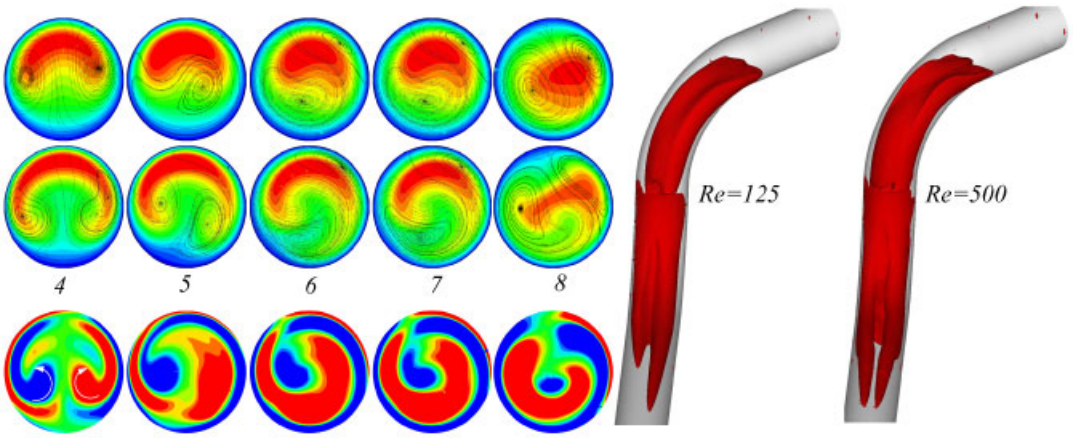


Figure 5. 45° model, $Re = 125\,500$: the isocontour shows the $\lambda_2$ coherent vortex structure highlighting the vortex patterns in each quarter bend. The inset sections correspond to the numbering in Figure 3(a). The top two slices are axial velocity at $Re = 125$ and 500, respectively. The bottom slices show axial vorticity at $Re = 500$.

Initially considering Sections 1–4 which are within the first-quarter toroidal bend, we observe that two counter rotating vortices are established, these are the well-known Dean's vortices [14]. Directly associated with these secondary vortices is a displacement of the axial velocity profile towards the outside of the bend due to the centripetal force associated with the toroidal geometry. This type of pattern is established in the first bend of all configurations. However the increase in Reynolds number, which necessarily also increases the Dean number leads to a more energetic secondary flow and a larger associated crescent shape in the axial flow profile.

Sections 5–9 of Figure 4 show the sectional profile during the second bend where the curvature has now been reversed. We observe that the reverse curvature of the second bend first overcomes the initial Dean vortex pattern of the first bend and then establishes a new Dean vortex pattern (of opposite rotation) by Section 9. This is also shown in the $\lambda_2$ isocontour. A similar trend is seen at both $Re = 125$ and $R = 500$. This is in contrast to the work of Pitt [44] where a double bend of similar curvature of radius but only a 45° sweep angle (i.e. an eighth of a toroidal bend) was investigated. With a reduced sweep angle at a Reynolds number of $Re = 500$, the initial Dean vortices were able to overcome the influence of the second bend.

In Figure 5, we show similar data to that in Figure 4 but for the 45° model geometry again at $Re = 125$ and 500. In this configuration, a similar Dean vortex pattern is established in the first bend. However when we introduce a 45° non-planarity during the second bend, the rotation of the non-planar bend enhances one of the Dean vortices and diminishes the other. This is particularly evident in the $\lambda_2$ isocontour for the $Re = 125$ case where we observe that one of the Dean vortices within the outflow region is longer than the other.

It is interesting to note that increasing the Reynolds number (and implicitly the Dean number) reduces the asymmetry of the $\lambda_2$ isocontours within the outflow and leading to a similar type pattern to the $\lambda_2$ isocontour shown in Figure 4. However, the axial vorticity plots shown in the bottom series in Figure 5 demonstrate that mixing is still present at this Reynolds number. The initial rotation of the vortices is indicated in the plot of Section 4.



DOI: 10.1002/fld

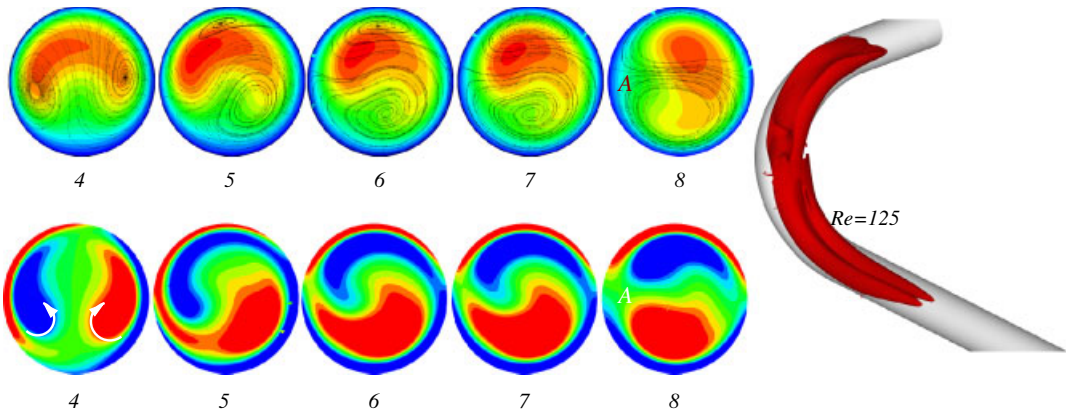


Figure 6. 90° model, $Re = 125$: the isocontour shows the $\lambda_2$ coherent vortex structure highlighting the two Dean vortex patterns set up in each quarter bend. The inset sections correspond to the numbering in Figure 3(a).

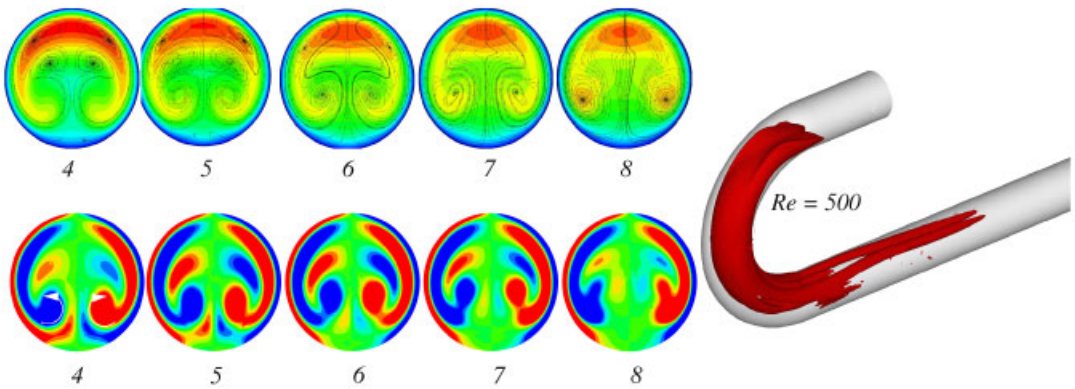


Figure 7. 180° model, $Re = 500$: the isocontour shows the $\lambda_2$ coherent vortex structure highlighting the two Dean vortex patterns set up in each quarter bend. The inset sections show the axial velocity (top) and vorticity (bottom) and the numbering is consistent with Figure 3(a).

We next continue to increase the non-planarity and consider the 90° geometry as shown in Figure 6 at $Re = 125$. Unlike the 45° model at this Reynolds number, shown in Figure 5, we observe that the Dean vortices do not show the asymmetry in the $\lambda_2$ pattern. Although we observe some realignment of the first bend Dean vorticity between Sections 4 and 5 very rapidly the second toroidal bend establishes a Dean vortex pattern consistent with the bend's curvature. By Section 8 two Dean vortices are established and we note that point $A$ is now located at the top of the outflow branch making the vortices consistent with the $\lambda_2$ isocontours.

The next level of non-planarity was the 135° model which has similar dynamics to those as observed in the 45° model and so we shall not consider it further here. In Figure 7 however we consider the 180° model. This model is a half a toroidal geometry and therefore is analogous to a



DOI: 10.1002/fld

classical Dean flow throughout the geometry. One significant point of interest at $Re = 500$ however is highlighted in the secondary flow patterns between Sections 4 and 6 where we observe that the strength of the primary Dean vortices are sufficient to lead to secondary eruption of vorticity from the wall which is also wrapped around the primary vortices to create an internal set of vortices. A tertiary set of vorticies can also be observed in secondary streamlines at the bottom of Sections 4 and 5. As we progress down the pipe, the vortices merge and annihilate leaving a weaker set of vortices at the pipe outflow.

## 6. CONCLUSIONS

The steady flow patterns observed in the idealized non-planar double bend geometries at $Re = 125$ and 500 have been investigated by consideration of how the primary and the transverse flows are affected by curvature, non-planarity and Reynolds number. The analysis highlights the complex and sometimes intricate secondary flow patterns which are possible within these types of configurations at physiologically relevant parameters.

During the first-quarter toroidal, a Dean vortex pattern is established. In the planar configurations investigated, we observed that in the double bend (0° model) the local curvature of each separate bend ultimately dictates the Dean pattern in each bend. Within the half-toroidal (180°) model, we observed the generation of secondary and tertiary vortex pattern at $Re = 500$ due to a boundary layer eruption promoted through the strength of the primary vortices.

The introduction of 45° and 135° non-planarity cause a strengthening of one of the Dean vortices and associated weakening of the other vortex. Increasing the Reynolds number in these configurations leads to a more rapid realignment of the vortices and a more symmetric Dean vortex configuration during the outflow region. A larger degree of non-planarity, as in the 90° model, does not enhance this mechanism but rather leads to a more symmetric Dean vortex patterns. Therefore as a final conclusion, we note that there appears to be an optimal non-planar angle to achieve asymmetry in the Dean vortex pattern.

ACKNOWLEDGEMENTS

The authors would like to acknowledge the support of the Henry Smith's Kensington Estate Charity and partial computing support under the EPSRC Turbulence Consortium. The last author would also like to acknowledge partial support from an EPSRC Advanced Research Fellowship.

REFERENCES

1. Bierman BL. Atherosclerosis and aging. *Federation Proceedings* 1978; **37**:2832–2836.
2. Ross R, Harker L. Hyperlipidemia and atherosclerosis: chronic hyperlipidemia initiates and maintains lesions by endothelial cell desquamation and lipid accumulation. *Science* 1976; **193**:1094–1100.
3. Small DM. Progression and regression of atheroscleroic lesions: insights from lipid physical biochemistry. *Arteriosclerosis Thrombosis and Vascular Biology* 1988; **8**:103–129.
4. Roach MR, Fletcher J, Cornhill JF. The effect of the duration of cholesterol feeding on the development of sudanophilic lesions in the rabbit aorta. *Arteriosclerosis Thrombosis and Vascular Biology* 1976; **25**:1–11.
5. Schwenke DC, Carew TC. Initiation of atherosclerotic lesions in cholesterol-fed rabbits. I. Focal increases in arterial ldl concentration precede development of fatty streak lesions. *Arteriosclerosis Thrombosis and Vascular Biology* 1989; **9**:895–907.



DOI: 10.1002/fld

6. Gentile AT, Mills JL, Gooden MA, Westerband A, Cui H, Berman SS, Hunter GC, Hughes JD. Identification of predictors for lower extremity vein graft stenosis. *American Journal of Surgery* 1997; **174**:218–221.
7. Davies JG, Kim JH, Klyachkin ML, Barber L, Dalen H, Svendsen E, Carson CC, Hagen PO. Diabetes mellitus and experimental vein graft structure and function. *Journal of Vascular Surgery* 1994; **19**:1031–1043.
8. Reddan DN, Marcus RJ, Owen WF, Szczech LA, Landwehr DM. Long-term outcomes of revascularization for peripheral vascular disease in end-stage renal disease patients. *American Journal of Kidney Diseases* 2001; **38**:57–63.
9. Davies PF. Flow-mediated endothelial mechanotransduction. *Physiological Reviews* 1995; **75**:519–560.
10. Ku DN, Giddens DP, Zarins CK, Glagov S. Pulsatile flow and atherosclerosis in the human carotid bifurcation. *Arteriosclerosis Thrombosis and Vascular Biology* 1985; **5**:293–302.
11. Tardy Y, Resnick N, Nagel T, Gimbrone MA, Dewey CF. Shear stress gradients remodel endothelial monolayers in vitro via a cell proliferation migration loss cycle. *Arteriosclerosis Thrombosis and Vascular Biology* 1997; **17**: 3102–3106.
12. Dean W. Note on the motion of fluid in a curved pipe. *Philosophical Magazine* 1927; **20**:208–223.
13. Dean W. Note on the motion of fluid in a sinuous channel. *Philosophical Magazine* 1927; **17**:912–925.
14. Dean W. The streamline motion of fluid in a curved pipe. *Philosophical Magazine* 1928; **30**:673–693.
15. John E. Flow of water in curved pipes. *Proceedings of the Royal Society*, *Series A* 1910; **84**:107–118.
16. John E. Experiments of streamline motion in curved pipes. *Proceedings of the Royal Society*, *Series A* 1912; **85**:119–131.
17. Back LH, Back MR, Kwack EY, Crawford DW. Flow measurements in a human femoral artery model with reverse lumen curvature. *Journal of Biomechanical Engineering—Transactions of the ASME* 1998; **110**:300–309.
18. Back LH, Kwack EY, Crawford DW. Flow measurements in an atherosclerotic curved, tapered femoral artery model of man. *Journal of Biomechanical Engineering—Transactions of the ASME* 1998; **110**:310–319.
19. Banerjee RK, Cho YI, Back LH. Numerical studies of three-dimensional arterial flows in reverse curvature geometry: Part I—peak flow. *Journal of Biomechanical Engineering—Transactions of the ASME* 1993; **115**: 316–329.
20. Wada S, Karino T. Theoretical prediction of low-density lipoproteins concentration at the luminal surface of an artery with a multiple bend. *Annals of Biomedical Engineering* 2002; **30**:778–791.
21. Caro CG, Doorly DJ, Tarnawski M, Scott KT, Long Q, Dumoulin CL. Non-planar curvature and branching of arteries and non-planar-type flow. *Proceedings of the Royal Society*, *Series A* 1996; **452**:185–197.
22. Caro CG, Fitzgerald JM, Schroter RC. Atheroma and arterial wall shear: observations, correlation and proposal of a shear dependent mass transfer mechanism for atherogenesis. *Proceedings of the Royal Society*, *Series B* 1971; **177**:109–159.
23. Farthing S, Peronneau P. Flow in the thoracic aorta. *Cardiology Research* 1979; **13**:607–620.
24. Paulsen PK, Hasenkam JM. Three-dimensional visualization of velocity profiles in the ascending aorta in dogs, measured with a hot-film anemometer. *Journal of Biomechanics* 1983; **16**:201–210.
25. Frazin LJ, Lanza G, Vonesh M, Khasho F, Spitzzeri C, McGee S, Mehlman FD, Chandran KB, Talano J, McPherson D. Functional chiral asymmetry in descending thoracic aorta. *Circulation* 1990; **82**:1985–1994.
26. Yearwood TL, Chandran KB. Physiological pulsatile flow experiments in a model of the human aortic arch. *Journal of Biomechanical Engineering* 1984; **15**:683–704.
27. Kilner PJ, Yang GZ, Mohiaddin RH, Firmin DN, Longmore DB. Helical and retrograde secondary flow patterns in the aortic arch studied by three-directional magnetic resonance velocity mapping. *Circulation* 1993; **88**:2235–2247.
28. Hoydu AK, Bergey PD, Haselgrove JC. Mri bolus tagging method for observing helical flow in the descending aorta. *Magnetic Resonance in Medicine* 1994; **32**:794–800.
29. Batten JR, Nerem RM. Model study of flow in curved and planar arterial bifurcations. *Cardiology Research* 1982; **16**:178–186.
30. Altobelli SA, Nerem RM. An experimental study of coronary artery fluid mechanics. *Biomechanical Engineering* 1985; **107**:16–23.
31. Sabbah HN, Walburn FJ, Stein PD. Patterns of flow in the left coronary artery. *Journal of Biomechanics* 1984; **106**:272–279.
32. Moore JE, Maier SE, Ku DN, Biesiger P. Haemodynamics in the abdominal aorta: a comparison of in vitro and in vivo measurements. *Journal of Applied Physiology* 1994; **76**:1520–1527.
33. Back MR, Cho YI, Back LH. Fluid dynamic study in a femoral artery branch casting of man with upstream main lumen curvature for steady flow. *Journal of Biomechanical Engineering* 1985; **107**:240–248.
34. Scholten FG, Wensing PJW. Atherogenesis in the distal part of the femoral artery: a functional anatomical study of local factors. *Ph.D. Thesis*, University of Utrecht, 1995.




DOI: 10.1002/fld

35. Giordana S, Sherwin SJ, Peiró J, Doorly DJ, Crane JS, Lee KE, Cheshire NJW, Caro CG. Local and global geometric influence on steady flow in distal anastomoses of peripheral by-pass grafts. *Journal of Biomechanical Engineering—Transactions of the ASME* 2005; **127**:1087–1098.
36. Lu Y, Lu X, Zhuang L, Wang W. Breaking symmetry in non-planar bifurcations: distribution of flow and wall shear stress. *Biorheology* 2002; **39**:431–436.
37. Sherwin SJ, Shah O, Doorly DJ, Peiró J, Papaharilaou Y, Watkins N, Caro CG, Dumoulin CL. The influence of out-of-plane geometry on the flow within a distal end-to-side anastomosis. *Journal of Biomechanical Engineering* 2000; **122**:86–95.
38. Perktold K, Florian H, Hilbert D, Peter R. Wall shear stress distribution in the human carotid siphon during pulsatile flow. *Journal of Biomechanics* 1988; **21**:663–671.
39. Jeong J, Hussain F. On the identification of a vortex. *Journal of Fluid Mechanics* 1995; **285**:69–94.
40. McDonald AD. *Blood Flow in Arteries*. Edward Arnold: Paris, 1974.
41. Peiró J, Sayma AI. A 3-D unstructured multigrid Navier–Stokes solver. In *Numerical Methods for Fluid Dynamics V*, Morton KW, Baines MJ (eds). Oxford University Press: Oxford, 1995.
42. Karniadakis GE, Sherwin SJ. *Spectral/hp Methods for CFD*. Oxford University Press: Oxford, 1999.
43. Melander M, Hussain F. Understanding turbulence via vortex dynamics. *The Lumley Symposium Studies in Turbulence*. Springer: Berlin, 1991; 157–178.
44. Pitt R. Numerical simulation of fluid mechanical phenomena in idealised physiological geometries: stenosis and double bend. *Ph.D. Thesis*, Imperial College London, University of London, 2005.



DOI: 10.1002/fld